Journal of Heat Transfer. Received August 10, 2018;
Accepted manuscript posted April 24, 2019. doi:10.1115/1.4043572

A high temperature instrument for consecutive measurements of thermal conductivity, electrical conductivity, and Seebeck coefficient

Sajad Yazdani,[1,†,#] *Hyun-Young Kim,*[1,‡,#] *and Michael Thompson Pettes*[1,2,]*

[1]Department of Mechanical Engineering, University of Connecticut, Storrs, Connecticut 06269, USA.

[2]Center for Integrated Nanotechnologies (CINT), Materials Physics and Applications Division, Los Alamos National Laboratory, Los Alamos, New Mexico 87545, USA

[#]These authors contributed equally.

*Corresponding author, email: pettesmt@lanl.gov

Abstract

A device for measuring a plurality of material properties is designed to include accurate sensors configured to consecutively obtain thermal conductivity, electrical conductivity, and Seebeck coefficient of a single sample while maintaining a vacuum or inert gas environment. Four major design factors are identified as sample-heat spreader mismatch, radiation losses, parasitic losses, and sample surface temperature variance. The design is analyzed using finite element methods for high temperature ranges up to 1000°C as well as ultra-high temperatures up to 2500°C. A temperature uncertainty of 0.46% was estimated for a sample with cold and hot sides at 905.1 and 908.5°C, respectively. The uncertainty at 1000°C was calculated to be 0.7% for a ΔT of 5°C between the hot and cold sides. The thermal conductivity uncertainty was calculated to be -8.6% at ~900°C for a case with radiative gains, and +8.2% at ~1000°C for a case with radiative losses, indicating the sensitivity of the measurement to the temperature of the thermal guard in relation to

the heat spreader and sample temperature. Lower limits of -17 and -13% error in thermal conductivity measurements were estimated at the ultra-high temperature of ~2500°C for a single-stage and double-stage radiation shield, respectively. It is noted that this design is not limited to electro-thermal characterization and will enable measurement of ionic conductivity and surface temperatures of energy materials under realistic operating conditions in extreme temperature environments.

Keywords

Conduction, Energy Systems, Experimental Techniques, Micro/nanoscale Heat Transfer, Thermophysical Properties

Introduction

Obtaining accurate knowledge of temperature-dependent physical properties of manufactured materials has significantly broad implications in various industries. Measurements of thermal, electrical, and ionic conductivity are essential for practical use of newly developed materials including new chemistries and morphologies [1-8] or engineered isotopic makeup [9-14] and can affect the quality control aspects needed for the integrity of energy storage and conversion systems in particular. High-confidence measurements become more critical at high temperatures (above 400°C) where obtaining accurate measurements of thermophysical properties, becomes more complicated and challenging due to significant parasitic losses. Combined measurements of electrical and thermal properties have focused on thermoelectric energy conversion for historical reasons where accuracy requirements are most stringent [15-17]. For this application area, thermal-to-electrical energy interconversion holds the potential to convert unused streams of thermal energy, offering improved reliability with no moving parts, smaller size, longer operational lifetime, and thermal efficiencies on the order of 5–10% [3, 18, 19]. The laws of nature do not dictate an upper limit on the performance metric of thermoelectric materials, and thus with improvements in materials design this technology is capable of achieving one third of the Carnot efficiency [1], deemed the definition of a "practical system" by the U. S. Department of Energy [20]. However, the current conversion efficiencies are too low for practical applications. The efficiency is related to the dimensionless figure of merit zT [21]. There are three material properties that figure into zT: (1) electrical conductivity, σ, (2) thermopower (Seebeck coefficient), S, and (3) thermal conductivity, κ. Currently, all three properties are measured in different instruments, at different times, and requiring different materials. The problem arises, however, if an instrument is inaccurate or has an excessive measurement error. A round-robin study of Seebeck coefficient

measurements for un-doped Bi_2Te_3 and constantan at 100°C found variations of approximately 4% and 6%, respectively [15]. A round-robin study of the Seebeck coefficient and electrical resistivity of Bi_2Te_3 and $Bi_{0.5}Sb_{1.5}Te_3$ revealed measurement errors of about 5.5% for Seebeck coefficient and 12.5% for the electrical resistivity on the first round, and 4% for Seebeck coefficient and 5% to 9% for the electrical resistivity on the second round [17]. This indicates the level of uncertainty present in the instruments currently used to measure σ and S. If an instrument's results vary too widely from these margins, or exhibits excessive measurement error, then its results may lose some significance leading to failure of reproducibility in high zT reports. While the errors for individual properties may remain within an acceptable range, when converted into zT the propagated error can become excessive. Indeed, a round-robin study for all thermoelectric properties revealed a variation in zT ranging from 12 to 16%, from temperature ranges of ~20 to 500°C due to the large error in its component properties [22]. The problem is further exacerbated when different measurement instruments are used for each of the component properties, as this not only combines the errors in each of the instruments, but may also require different sample preparations, degradation of the samples, or use of multiple samples in general.

There are several problematic complications in existing experimental methods used to obtain zT, which remain relevant to all application areas where high temperature electrical and thermal property determination are critical. The electrical conductivity of cylindrical pellet samples can be measured using the van der Pauw method [23]. This method, however, cannot be integrated with Seebeck or thermal conductivity measurements, as the voltage and current leads must be attached from the sides. During Seebeck and thermal conductivity measurements, this will introduce an additional parasitic heat loss that will distort the temperature gradient. This cannot be mitigated by attaching the leads to a radiation shield, since the electrical contacts will be touching

a non-uniform range of temperatures. Thus, van der Pauw methods must be performed in a separate portion of the instrument or using an outside instrument altogether. García-Cañadas and Min [24] arranged an apparatus for measuring electrical resistivity via the van der Pauw method as well as Seebeck coefficient at room temperatures. The Seebeck coefficient was measured by using only two probes directly in contact with the sample in order to read the voltage and temperature difference along the two points of contacts [24]. The assumption in using such a configuration is that microstructure, temperature distribution and, therefore, Seebeck coefficient is highly homogenous across the sample [25]. Thus, using such methods is only appropriate for obtaining rough evaluation of Seebeck coefficient at low temperatures. Another useful method reported by Kraemer and Chen [26] involves running a current directly through a sample, using current leads embedded in the thermoelectric block. A square-wave alternating current is used to negate thermoelectric contributions to the measured voltage drop, and both the heaters and the radiation shield are held at a desired temperature for measuring a desired property. The voltage fluctuation is then measured with a lead possessing a low Seebeck coefficient (niobium), and resistivity can be calculated as shown in Ref. [26]. The major concern, however, is determining the effects that arise from non-uniform current distribution through the heat spreader and the electrical contact resistance. This is more concerning for instruments where thermocouples do not directly touch the sample.

Although other techniques have been used, the most common scheme to obtain zT involves three separate measurements on three separate instruments: (i) electrical conductivity and thermopower are obtained by an Ulvac ZEM-3 instrument for a single rectangular bar or cylinder of material, (ii) thermal diffusivity, α, is measured using a Netzsch Laser Flash Apparatus (LFA) for a single cylindrical pellet, and (iii) the specific heat capacity, c, is measured using a Netzsch

Differential Scanning Calorimetry (DSC) instrument for a single cylindrical pellet. The thermal conductivity is obtained from (ii) and (iii) as $\kappa = \alpha\rho c$, where ρ is the mass density. As for existing commercial instruments for thermoelectric property measurements, the ULVAC ZEM-3 measures the Seebeck coefficient by setting a temperature gradient across two contact points along the height of a long rectangular or cylindrical sample, and the electrical conductivity by pulsing an electrical current through the sample. It then measures the voltage response using two thermocouples/voltage probes along the sample sides to extract S and σ. By measuring at the sample sides in a four-probe off-axis geometry, this avoids the additional contact resistances present in two-point geometries in which the probes are embedded in the contacts. A thermal finite element analysis by Mackey *et al.* [27] showed, however, that these parasitic conduction pathways resulted in an error of up to -13.1% at high temperature ranges for the Seebeck coefficient. A major contributor to this error was the cold-finger effect, in which the probes at sample sides leeched heat away from the sample and thus distorted the temperature gradient. As a solution for this effect, Snyder *et al.* [28, 29] developed an instrument in which the probes were inserted axially through the contacts and onto the sample surface, thereby avoiding both the contact resistance and the cold finger effect. In their design, a crossed-wire thermocouple configuration composed of niobium and chromel wires were used at temperatures up to ~652°C. The thermocouple wires were threaded through a 4-bore ceramic tube, and the ceramic tube was in turn heat-sunk to the heaters in order to minimize cold-finger effects. This axial arrangement of thermocouples minimizes errors in S at high temperatures by solving the cold finger effect problem, as validated by a recent finite element analysis [30], however this method lacks the capability to measure electrical or thermal properties. Thermal properties are currently obtained from thermal diffusivity measurements conducted using transient laser flash diffusivity methods and specific heat is measured using differential scanning

calorimetry (DSC). A round-robin investigation of these measurements by Wang and co-workers [17] revealed that thermal conductivity measurements contributed the greatest share in the overall uncertainty of the measured zT. Two sets of round-robin investigations were conducted on *n*-type Bi_2Te_3 and *p*-type Bi_2Te_3-Sb_2Te_3 alloy with thermal properties measured using Netzsch LFA447 and LFA457 laser flash systems, TA Instruments/Anter Flashline 5000 and XPlatform for thermal diffusivity measurements, and three types of Netzsch DSCs, a TA Instruments DSC, and Quantum Design Physical Properties Measurement System (PPMS) for specific heat measurements. The thermal diffusivity measurements showed the largest variation between measurements of ±15% to ±17% at ~200°C. Interestingly, DSC measurements posed the biggest reproducibility challenge with more than ±15% scatter in the combined data at temperatures up to ~230°C. One main challenge arose from the unstable baselines changing between DSC equipment. The results showed more than ±15% scatter in the measured specific heat values over a temperature range from ~20–200°C. The results from seven laboratories on 14 samples indicated that the DSC measurement is the most operator-dependent measurement and least likely to produce reliable data. The data scatter for the thermoelectric figure of merit was ±6.8% near room temperature and ±17.1% at 200°C. Lacking the capability for reliable and accurate measurements of the electro-thermal properties is even worse at higher temperatures above those investigated in the round-robin study [17]. On the other hand, the currently available steady state methods for direct thermal conductivity measurements are not rigorous enough to be employed for elevated temperatures. Thus, there is a critical need for new designs with improved capabilities. Configurations for different competing electrical and thermal property characterization methods are given in Figure 1.

In the present work, we propose a new instrument design for accurate and consecutive measurements of temperature-dependent thermal and electrical conductivities as well as Seebeck coefficient at high temperatures (1000°C and above). The embedded axial thermocouple configuration designed by Snyder [28, 29] is adopted and new modifications and arrangements are proposed to enable consecutive measurements thermal and electrical properties in a single instrument. Additionally, another configuration is introduced and analyzed with potential capabilities to provide reliable measurements of these properties at an ultra-high temperature of 2500°C. The current work demonstrates a unique implementation of the measurements at such temperature ranges with capabilities to measure all the electrical and thermal properties consecutively on the same sample without the need for breaking the vacuum or inert gas environment, making it more suitable for high-throughput measurements or quality-control processes. Although outside the scope of this work, we note that the proposed design is also capable of obtaining *in operando* electro-chemical property data without modification.

Uncertainty analysis of the Snyder design for Seebeck coefficient measurement

In a previous investigation [30], we performed a thermal analysis of the Snyder design [28, 29] for Seebeck coefficient measurements using the finite element method. The key feature in that design is axially inserted thermocouples which are thermally anchored to the heating blocks and in direct contact with the sample. Herein, we report the uncertainty values of the Snyder design due to temperature non-uniformity (on the hot and cold surfaces of the sample) and the cold-finger effect as well as the overall uncertainty for two cases – with and without geometry mismatch between the sample and heat spreaders. Modeling details and geometry used for this analysis are given in Ref. [30]. Two types of uncertainties were considered: (i) the uncertainty due to non-

uniform temperature distribution on the top and bottom surfaces of the sample where the temperatures are measured by the axial thermocouples and (ii) the uncertainty due to the cold-finger effect. The former is caused by contact thermal resistances and the radiation heat loss from the outer surface of the sample. It is noted that the results are calculated for a pyroceram sample assuming an isotropic thermal conductivity of 2.82 $Wm^{-1}K^{-1}$ at 900°C and emissivity values obtained from Thermophysical Properties of Matter handbooks [31]. The uncertainty due to surface temperature distribution was calculated based on

$$U_T = \frac{(T_{\text{hot,average}} - T_{\text{cold,average}}) - (T_{\text{hot,measured}} - T_{\text{cold,measured}})}{(T_{\text{hot,measured}} - T_{\text{cold,measured}})}, \quad (1)$$

where $T_{\text{hot,average}}$ and $T_{\text{cold,average}}$ are the average of the top (hot) and bottom (cold) surfaces of the sample, respectively. Average temperatures were used since the maximum and minimum temperatures vary significantly due to some specifics related to the Synder design which would yield unreasonably large temperature uncertainties. $T_{\text{hot,measured}}$ and $T_{\text{cold,measured}}$ are the calculated temperatures of the sample center on the hot and bottom surfaces, respectively, where the temperatures are measured by the axial thermocouples. The uncertainty due to the cold-finger effect was calculated according to

$$U_{\text{cold-finger}} = \frac{(T_{\text{hot\_j2}} - T_{\text{cold\_j2}}) - (T_{\text{hot\_j1}} - T_{\text{cold\_j1}})}{(T_{\text{hot\_j1}} - T_{\text{cold\_j1}})}, \quad (2)$$

where $T_{\text{hot\_j1}}$, $T_{\text{hot\_j2}}$, $T_{\text{cold\_j1}}$, and $T_{\text{cold\_j2}}$ are the average temperature of the first (niobium thermocouple wire-sample interface) and second (niobium thermocouple wire-chromel thermocouple wire interface) cross-geometry thermocouple junctions on the hot and cold sides, respectively. The average values were calculated on the junction surfaces. The two niobium-

chromel junctions are used for voltage and temperature measurements on each side. The overall uncertainty was obtained by

$$U_{\text{total}} = \sqrt{(U_T)^2 + (U_{\text{cold-finger}})^2}\ , \tag{3}$$

where U_T and $U_{\text{cold-finger}}$ were calculated based on Equations 1 and 2, respectively.

In order to identify the effects of the sample being in a different diameter than the heat spreader, the analysis was performed for $r_{\text{sample}}/r_{\text{heat\_spreader}} = 0.42$ and 1 where r_{sample} and $r_{\text{heat\_spreader}}$ refer to the radius of the sample and the heat-spreader, respectively. For the case $r_{\text{sample}}/r_{\text{heat\_spreader}} = 1$, the results showed uncertainty values of 8.7% and 0.4% caused by a surface temperature non-uniformity and cold-finger effect, respectively for hot side and cold side average surface temperatures of 905.8°C and 900.6°C, respectively. The overall uncertainty was calculated to be 8.7%. The calculated cold-finger uncertainty contributes only ~4.6% to the total uncertainty and shows the very effective suppression of the cold-finger effect by using axially embedded thermocouples in the Snyder design [28, 29]. This is 32.5 times lower than the 13% cold-finger uncertainty value obtained for the Ulvac ZEM-3 at a similar temperature of 917°C [27]. As the temperature of the hot side in our analysis was raised to 912.7°C to approximate a 10°C temperature drop across the sample, the uncertainty values remained fairly constant. The analysis for the case $r_{\text{sample}}/r_{\text{heat\_spreader}} = 0.42$ (sample smaller in diameter than the heat-spreaders, r_{sample} = 25 mm, $r_{\text{heat\_spreader}}$ = 60 mm), larger uncertainty values of 10.1, 1.0, and 10.2% were estimated for the surface temperature distribution, cold-finger, and overall uncertainty, respectively for a case with average sample surface temperatures of 905.9°C and 900.9°C. Table 1 summarizes the uncertainly analysis for the Snyder design.

Description of instrument geometry

In order to analyze the uncertainty in the electro-thermal transport property measurements of the high temperature apparatus shown in Figure 2, a finite element model of the instrument was produced. A 12.7 mm-diameter, 5 mm-thick pellet sample was used for the modeling. Two tungsten heat spreaders were placed at the top and the bottom of the sample, with diameters of 12.7 mm and height of 40 mm each, with a 0.25 mm-thick sheet of grafoil® in between matching the sample diameter. Rectangular bars of 1.7 × 3 × 30 mm were used in place of cartridge heaters, with three heaters embedded into each of the heat spreaders symmetric about the center axis. Two 1.5875 mm-diameter and 65 mm in height alumina tubes were inserted through the center of the heat spreaders and onto the surfaces of the grafoil® sheets at the top and the bottom. Two 0.1 mm-thick leads of tungsten and niobium were then threaded through the alumina tubing and embedded into the grafoil® sheets. Three thin-walled cylinders of alumina with 3.175 mm diameter and 0.88 mm wall thickness were each placed axis-symmetrically on the top and the bottom heat spreaders. Tungsten wires of 0.2 mm diameter were attached to the outer surface of each of the cartridge heaters, while two 1.6 mm-diameter thermocouple probes were embedded into each of the heat spreaders. All of the wires, probes, insulating tubing, niobium and chromel thermocouple leads, and insulating cylinders were made to terminate 25 mm from the top and the bottom edges of the heat spreaders. The entire model was setup with a bilateral symmetry. The simulation was run for base temperatures between 100 and 1000°C. The support ends and wire ends for the hot side heat spreader were set at 5°C higher than the base temperature assuming they were sunken into the second stage heating platform, while cold ends were set at 25°C. The bisected surfaces were assumed to be adiabatic due to symmetry. All other exposed surfaces were set with the radiation boundary condition with surrounding temperatures matching the hot-side temperature. Both lower and upper heaters were then adjusted to produce a desired temperature drop from the hot-side

temperature to the base temperature at the center of the sample. It was assumed that the wires and supporting columns were electrically insulated enough for an open circuit condition, and therefore any thermoelectric effects were neglected in the model. It was assumed that the entire system was placed in a vacuum condition with no convective heat transfer, and the contacts were assumed to possess negligible resistances. Thermal conductivities and emissivities for the all the materials were estimated using the Thermophysical Properties of Matter handbooks [31]. The analyses were conducted on various sample materials of silicon dioxide, pyroceram 9606, boron nitride, and hafnia (HfO_2) with the same handbooks used for property values. Thermal conductivity values of pyroceram 9606 were adopted based on the data provided by NETZSCH group. The thermal conductivity of the grafoil® was estimated using product specifications from Graftech Inc. [32]. The entire model was discretized into 1.04×10^6 elements, and the Mechanical ANSYS APDL non-linear iterative solver was used. The outside perspective of the modeled apparatus and a detailed view of the inside arrangement are illustrated in Figure 2.

Finite element analysis of thermal conductivity measurement

By keeping track of the amount of heat flowing through the sample, q_{sample}, the same setup can also be used to measure thermal conductivity using the equation [33]

$$\kappa = -\frac{q''_{\text{heater\_output}} h_{\text{sample}}}{\Delta T A_{\text{cross-sectional}}}, \tag{4}$$

where h_{sample} and $A_{\text{cross-sectional}} = \pi r^2_{\text{sample}}$ are the height and cross-sectional area of the sample respectively, $q''_{\text{heater\_output}}$ is heat flux output by the cartridge heaters in the upper heat spreader, and ΔT is the temperature drop across the sample measured at the center point of the sample surfaces.

In existing thermal guard designs for a direct measurement of high temperature materials properties, the large heat losses in the instrument itself cause the power input to the heaters to vary wildly from the actual heat flow through the sample and therefore prevent their use in high-confidence thermal conductivity measurements. This is particularly relevant at higher temperatures, where the heat losses are magnified by the fourth-power term inherent to radiative losses. It is, however, possible to minimize the heat losses from one side of the instrument in order to estimate the amount of sample heat flux using the power supplied to the cartridge heaters. In order to minimize the conductive losses through the supporting columns and probes, using long and narrow geometry with low thermal conductivity materials is not enough, as the residual heat losses will directly contribute to the measurement error. Instead, a change can be implemented in which all columns and probes are sunk into a second heating stage with separately controlled heaters. This second stage can be set to the nominal temperature of the initial heating stage so that there will be a minimal temperature difference between the two stages. Combined with traditional usage of low cross-sectional areas, large lengths, and low thermal conductivity materials, this can help reduce the errors to an acceptable level as will be discussed.

While convective losses are not an issue due to the common usage of high vacuum environments, radiative losses can still cause significant problems with thermal conductivity estimation even with radiation shields in place. This problem is magnified in high temperature measurements. Two steps can be taken to alleviate these errors. First, the radiation shield temperature can be set at the nominal temperature of the sample hot side, rather than being fixed at the average temperature or at approximately similar temperatures. This requires more accurate control of the radiation shield temperature as well as the dynamic adjustment as the ΔT is varied during at each measurement. It does, however, significantly reduce radiation losses from the hot

side. This is due to the fact that even when the radiation shield is set at the nominal hot side temperature, there will be some temperature variation, and therefore radiative losses. Secondly, further reduction in losses can be achieved by having the radiation shield be made of a low-emissivity material for a passive shielding effect.

In our model, emissivities were adjusted to estimate the emissivity of the surrounding radiation shield by using the expression [33]

$$\varepsilon_{\text{eff}} = \left[\frac{1}{\varepsilon_{\text{surface}}} + \frac{r_{\text{o}}}{r_{\text{sheild}}} \left(\frac{1}{\varepsilon_{\text{shield}}} - 1 \right) \right]^{-1}, \tag{5}$$

where ε_{eff}, $\varepsilon_{\text{surface}}$, and r_{o}, are the effective emissivity, surface emissivity, outer surface radius of the objects (heat spreader, sample, support posts, wires, etc.), and $\varepsilon_{\text{shield}}$ and r_{shield} are the shield emissivity and shield radius, respectively. The ratio of the heat spreader radius to that of the tungsten shield is set to be 0.706. The temperature of the upper instrument surfaces where set to be 5°C above the nominal temperatures. The heater output was compared to the averaged heat flux through the sample and is presented in Table 2.

As expected, there is a tendency for there to be some heat loss from the upper heaters, and therefore the heat flux will be overestimated by ~2% at low temperatures and by up to ~7.6% at 1000°C. There is, however, a competing effect from the radiation on the sample itself which tends to increase the heat flux along the edges of the sample, especially in the lower half. This effect can be seen in Figure 3a,b for a sample at 300°C and 1000°C, respectively. Due to the fourth power term present in radiative heat transfer, the effect is about an order of magnitude larger in scale at 1000°C. The heat flux, however, remains more stable at the centers of the sample. The steepest increases in the heat flux are mostly in the lower edges, where they will have the lowest amount of impact on the measurement the temperature gradient is obtained at the center. Table 2 also

includes an average over the top surface of the sample, before the radiation on the sample can take effect. This shows that without the competing effect, the heat flux is overestimated from ~2.1% at low temperatures to ~12.8% at high temperatures. Since the heater losses are greater than the sample gains, higher emissivity samples as well as slightly larger temperature gradients should be tolerable without increasing the error significantly.

There is, however, a competing effect from the radiation on the sample itself which tends to increase the heat flux along the edges of the sample, especially in the lower half. This effect can be seen in Figure 3 for temperatures of 300°C and 1000°C. Due to the fourth power present in radiative heat transfer term, the effect is about an order of magnitude bigger in scale at the 1000°C limit. The heat flux remains more stable through the center of the sample. Instead, the steepest increases in the heat fluxes are mostly in the bottom edges, where they will have the lowest amount of impact on the measurement since it will have the least time to affect the temperature gradient, and the measurement is done at the center. Table 2 lists an average over the top surface of the sample, before the radiation on the sample can take effect. This shows that, without the competing effect which we have included in our model, the heat flux would be overestimated from 2.1% at low temperatures to 12.8% at high temperatures. Since the heater losses are greater than the sample gains, higher emissivity samples as well as slightly larger temperature gradients should be tolerable without increasing the error.

The thermal conductivity that would be measured in this case was calculated using Equation 4 and was compared with the input conductivity to obtain a relative error, as listed in Table 3. This was compared to the error propagated from the temperature probe error as well as the error between the input heat and the surface average. The two were found to be mostly in agreement, varying by at most 0.56% at 1000°C. The errors tended to overestimate the thermal

conductivity, with minimum of 2.1% at 100°C and 8.2% at high temperature 1000°C. From the propagated error, it can be seen that the heat flux is the dominant error source in the system. The heat flux uncertainty values were calculated by

$$U_{\text{heat\_flux}} = \frac{q''_{\text{full\_surface,average}}}{q''_{\text{heater\_output}}}, \tag{6}$$

Where $q''_{\text{full\_surface,average}}$ is the sample full top (hot-side) surface average heat flux. The upper limit of temperature difference uncertainty was calculated based on

$$U_{\Delta T} = \frac{(T_{\text{hot,max}} - T_{\text{cold,min}}) - (T_{\text{hot,measured}} - T_{\text{cold,measured}})}{(T_{\text{hot,measured}} - T_{\text{cold,measured}})}, \tag{7}$$

where $T_{\text{hot,max}}$ *and* $T_{\text{cold,min}}$ are the maximum and minimum temperatures on the upper (hot) and lower (cold) sample surfaces, respectively. $T_{\text{hot,measured}}$ and $T_{\text{cold,measured}}$ are the calculated temperatures of the sample center on the hot and cold surfaces, respectively, where the temperatures are measured by the axial thermocouples. The propagated thermal conductivity error was calculated based on

$$U_{\text{total}} = \sqrt{(U_{\text{heat\_flux}})^2 + (U_{\Delta T})^2}, \tag{8}$$

where $U_{\text{heat\_flux}}$ and $U_{\Delta T}$ are the heat flux and temperature uncertainty values, respectively. A summary of errors related to the measurement of thermal conductivity is given in Table 3. Note that for Table 3 the radiation shield was set to the nominal hot-side temperature and the upper instrument boundary condition was set to constant temperature 5°C above the nominal temperature, and hence radiative losses from upper heat spreader lead to an overestimation in the amount of heat passing through the sample.

Analysis of thermal conductivity measurement (insulating versus constant temperature upper instrument boundary condition)

The effects of the upper surface boundary condition shown in Figure 2b being insulating versus constant temperature is investigated. In reality, making a thermally insulating surface at such high temperatures can be quite challenging if not impossible. One solution is to add a heating block in contact with the support ends and wire ends on the hot side of the instrument forcing the temperature gradient, and thus the heat flux through the upper part of the instrument, to drop to near zero. The temperature of this heating block can be set by using thermocouples embedded in the block. Figure 4 demonstrates the temperature distribution across the instrument with a maximum temperature of 909°C, while the radiation shield is also kept at 909°C. The temperature distribution across the outer surface of the upper heat spreader is shown in Figure 4b. The maximum temperature variation across this surface was calculated to be 0.45°C even at a high temperature of ~900°C. This temperature gradient plays an important role in the uncertainty of measured thermal conductivity and needs to be kept small. This is due the fact that the radiation heat loss from the heat spreader is dominant compared to other surfaces on the top-half of the instrument. This emphasizes the importance of the temperature of the radiation shield being held at the nominal temperature of this surface.

Figure 5 illustrates the temperature distribution across the sample for the top (hot) and bottom (cold) surfaces. On both sides, the outer surfaces have higher temperatures due to the inward radiation flux from the slightly hotter radiation shield. The variations at the center of the sample are due to the axial thermocouples and their insulating alumina tubing. Figure 5d shows that the temperature variation across the sample is less than 0.01°C for both sides. Such a low temperature variation indicates the suppression of the cold finger effect based on the axial

thermocouple configurations embedded in the heating block [30]. The results were obtained for a sample made of pyroceram 9606 with a relatively low thermal conductivity of ~2.9 $Wm^{-1}K^{-1}$ at 907°C. Keeping the sample temperature variation at a minimum is essential for Seebeck coefficient and electrical resistivity measurements as the temperature variation contributes to the uncertainty, thereby contributing to the overall error for zT.

Figure 6 shows the temperature distribution across the thermocouples consisting of tungsten and niobium wires. For the top side, the colder side of the thermocouple is in contact with the sample causing the center of the sample to be at a slightly lower temperature which is the opposite of the bottom side. Maximum temperature variations below 0.02°C were obtained for the top and bottom thermocouple junctions. Such low variations highlight the elimination of the cold-finger effect by using axial thermocouples with cross-wire geometry introduced by Snyder [28-30].

The uncertainty values for the thermal conductivity measurement of the pyroceram 9606 sample have been listed in Table 4. Note that for Table 4 the radiation shield was set to a slightly higher temperature than the upper heat spreader and therefore the sample as well, hence radiative energy was imparted to the sample leading to an underestimation in the amount of heat passing through the sample. Errors of -7.7% and -8.6% were estimated for the adiabatic and $T = 915$°C upper instrument boundary conditions, respectively. It can be seen that even when the boundary condition is set ~8°C above the nominal sample temperature (chosen as an upper limit to demonstrate its influence), the error in κ increases only by 1% versus having a perfect insulating surface. Achieving a $\Delta T < 8$°C is quite practical using commercial temperature controller technologies. Thus, using an additional heating block contacting the support ends and wire ends is a feasible substitution for the ideal case of an insulating boundary condition.

Modified design for direct thermal conductivity measurement at an ultra-high temperature of 2500°C

The capability for direct thermal conductivity measurements at ultra-high temperature ranges above 1500°C and even 2000°C can be quite beneficiary from a quality-control stand point for technologies operating at extreme temperatures. A modified design for thermal conductivity measurement at 2500°C is discussed here. The tungsten-niobium thermocouple wires design is replaced with a tungsten-5% rhenium versus tungsten-26% rhenium combination. Such configuration is commercially available from OMEGA Engineering with an upper operating limit of 2760°C. The alumina tubing (melting point ~2070°C) is replaced with hafnium oxide (HfO_2) with a melting temperature of ~2810°C. The heat spreaders and the radiation shield are assumed to be made of tungsten (melting point ~3380°C). Therefore, the only materials used in the proposed instruments design for ultra-high temperature applications are tungsten, hafnium oxide (melting point ~2810°C) and tungsten-rhenium alloys (operating up to 2760°C). The sample is assumed to be made of boron nitride (melting point 3000°C) with a dimension of 12.7 mm in diameter and 5 mm in height. All the materials properties were adopted from the Thermophysical Properties of Matter handbooks [31]. The first challenge in this case is to create a temperature gradient across the sample. Because the proportionality of the radiation heat flux with the fourth power of temperature, even a small temperature difference creates a considerable flux from/to the radiation shield making temperature control challenging. To have a better control over the temperature gradient from the sample, the radiation shield is split into two sections, i.e. having a top and bottom shield with separate temperature control feedbacks. In practice, this can be made of two shields with embedded cartridge heaters each one covering half of the height of the instrument. Thermocouples need to be embedded in these shields for separate temperature controls. The

temperature of the radiation shield for the bottom half and the bottom heater power are used in order to control the temperature gradient between the top and bottom surface of the sample. Table 5 lists the heater powers and the temperature set points for top and bottom radiation shield. A temperature gradient of 4.4°C between the hot and cold sides of the sample is calculated for the heater power values and radiation shield temperature setpoints listed in Table 5. The performed analysis reveals an error of -17.2% the thermal conductivity measurement of the sample at an average temperature of 2497.8°C.

Figure 7 shows the temperature distribution across the sample hot and cold side surfaces. The maximum temperature variation was calculated to be less than 0.23°C. The temperature distribution of the instrument is shown in Figure 7d. An average heat flux of 8.95×10^{6} Wm^{-2} was calculated on the support ends and wire ends at the bottom (cooled side) of the instrument. This value determines the overall flux that is needed to be removed from the instrument. This value can be controlled by changing the temperature of the bottom shield as well as the lower heat spreader cartridge heaters.

Radiation loss from the top heat spreader to the radiation shield is a major contribution to the uncertainty of the thermal conductivity measurements. The challenge is that due to the thermal resistance on the top heat spreader, there exists a temperature gradient of ~2°C along the heat spreader itself. In such ultra-high temperature ranges, even, the smallest temperature difference between the top heat spreader and the top radiation shield can cause a major heat loss/gain. Thus, even though the radiation shield is set at the average temperature of the heat spreader, the heat loss is still considerable due to the fact that the top heat spreader is not a constant temperature surface. Two solutions can be proposed in order to suppress such a heat loss: the first one is to use a material with a very high thermal conductivity for the heat spreader design. Having a high thermal

conductivity material reduces the thermal resistance along the heat spreader, thereby the temperature gradient. There are, however, few machinable candidates suitable for such a high temperature ranges, and tungsten seems to be indeed a proper choice. The other solution is to design multi-stage top radiation shield. For the single shield, the temperature was set to 2502°C (average temperature of the heat spreader). For the double-stage shield, the temperatures were set to 2502.1 and 2500.9°C for the first and second stage, respectively. The error analysis for the double-stage shield has been listed in Table 6. It can be seen that the thermal conductivity measurement error of -17.2% for a single-stage radiation shield can be reduced to -13.3% by using a double-stage shield. An ideal situation is to use multiple stages depending on the height and temperature gradient of the heat spreader. A simpler alternative is to use a radiation shield with an optimum thickness in order to create a similar temperature gradient along the shield and the heat spreader as they both are made of the same material i.e. tungsten.

Conclusion

An instrument design for high temperature consecutive measurements of thermal conductivity, electrical conductivity, and Seebeck coefficient was presented. The system size was limited in order to prevent sample-heat spreader geometric mismatch error, which will result in a significant uncertainty if the sample has a more than ~1.5 times larger diameter than the heat spreader. The radiation shield temperature was set at the hot-side heat spreader temperature more for practical purposes than to reduce the error, as the related errors were similar for different possible configurations of radiation shield temperatures. Unavoidable parasitic losses from the axially inserted thermocouples were identified, although these can be reduced to manageable levels using an upper thermal guard. Finally, the temperature variation on the sample surface was reduced

to below ~0.2°C at 2500°C by utilizing a thermally conduction interface material to help spread out the heat. For a typical system, this all resulted in an overall error in measured thermal conductivity of between -8.6 and +8.2% at near 1000°C where the variation in uncertainty was found to strongly depend on minor changes in the temperature of the thermal guard in relation to the heat spreader and sample temperature. Lower limits of -17 and -13% error in thermal conductivity measurements were estimated at an ultra-high temperature of ~2500°C for single-stage and double-stage radiation shield designs, respectively. Only tungsten, hafnium oxide, and tungsten-rhenium (for thermocouple wires) materials were used in the modified design for such a high temperature range. The major contribution to the error was radiation heat loss from the upper heat spreader. An ideal situation was identified where the upper radiation shield and upper heat spreader possessed the same temperature gradient. Such an ideal case can be approximated by using a multi-stage radiation shield.

Finally, our finite element analysis of Snyder's [28, 29] axially inserted thermocouple design for measuring Seebeck coefficients estimated surface temperature distribution, cold-finger effect, and overall uncertainties of 8.7%, 0.4%, and 8.8% respectively for a cylindrical sample with cold and hot side temperatures of 905.8 and 912.8°C, respectively. The negligible cold-finger uncertainty proves the effectiveness of the axial thermocouple configuration developed by Snyder in suppressing the cold-finger effect compared to the estimated 13% uncertainty at 917°C for commonly used 4-point off-axis Seebeck measurement methods with thermocouples contacting the side of the sample [27].

Journal of Heat Transfer. Received August 10, 2018;
Accepted manuscript posted April 24, 2019. doi:10.1115/1.4043572

Nomenclature

$A_{\text{cross-sectional}}$ = sample cross-sectional area

c = specific heat capacity

h_{sample} = sample height, dimension parallel to heat flow

q_{sample} = heat flow through the sample

$q''_{\text{full\_surface\_average}}$ = sample full surface average heat flux

$q''_{\text{heater\_output}}$ = heat flux output by cartridge heaters

r_{o} = outer surface radius of the object of interest

$r_{\text{heat\_spreader}}$ = outer surface radius of the heat spreader

r_{sample} = outer surface radius of the sample

r_{sheild} = radiation shield inner radius

S = Seebeck coefficient

$T_{\text{cold,average}}$ = average sample cold surface temperature

$T_{\text{cold,measured}}$ = calculated sample cold surface center temperature

$T_{\text{cold,min}}$ = minimum temperature on the cold surface of the sample

$T_{\text{hot,average}}$ = average sample hot surface temperature

$T_{\text{hot,max}}$ = maximum temperature on the hot surface of the sample

$T_{\text{hot,measured}}$ = calculated sample hot surface center temperature

$T_{\text{hot\_j1}}$ = average temperature of the first hot-side cross-geometry thermocouple junction (wire-sample interface)

$T_{\text{hot\_j2}}$ = average temperature of the second hot-side cross-geometry thermocouple junction (wire-wire interface)

$T_{\text{cold\_j1}}$ = average temperature of the first cold-side cross-geometry thermocouple junction (wire-sample interface)

T_{hot_j2} = average temperature of the second cold-side cross-geometry thermocouple junction (wire-wire interface)

$U_{cold\text{-}finger}$ = uncertainty due to the cold-finger effect

U_{heat_flux} = heat flux uncertainty

U_T = surface temperature distribution uncertainty used in the Snyder design model

U_{total} = overall uncertainty

$U_{\Delta T}$ = uncertainty in surface temperature difference between sample hot and cold surfaces

zT = thermoelectric figure of merit

α = thermal diffusivity

ΔT = temperature drop across the sample calculated at the center of the hot and cold surfaces

ε_{eff} = effective surface emissivity of an object in the presence of a radiation shield

ε_{shield} = surface emissivity of the radiation shield

$\varepsilon_{surface}$ = surface emissivity of the object

κ = thermal conductivity

ρ = mass density

σ = electrical conductivity

Acknowledgments

This work was performed, in part, at the Center for Integrated Nanotechnologies, an Office of Science User Facility operated for the U.S. Department of Energy (DOE) Office of Science. Los Alamos National Laboratory, an affirmative action equal opportunity employer, is managed by Triad National Security, LLC for the U.S. Department of Energy's NNSA, under contract 89233218CNA000001. This work was partially supported by the National Science Foundation

under Grant No. CAREER-1553987 (M.T.P., S.Y.), the UConn Research Foundation award number PD17-0137 (M.T.P., S.Y.), and a GE Graduate Fellowship for Innovation (S.Y.).

References

[1] Yazdani, S., and Pettes, M. T., 2018, "Nanoscale Self-Assembly of Thermoelectric Materials: A Review of Chemistry-Based Approaches," Nanotechnology, 29(43), pp. 432001-1–43. http://dx.doi.org/10.1088/1361-6528/aad673

[2] Pettes, M. T., Kim, J., Wu, W., Bustillo, K. C., and Shi, L., 2016, "Thermoelectric Transport in Surface- and Antimony-Doped Bismuth Telluride Nanoplates," APL Materials, 4(10), pp. 104810-1−9. http://dx.doi.org/10.1063/1.4955400

[3] Zhang, Q. H., Huang, X. Y., Bai, S. Q., Shi, X., Uher, C., and Chen, L. D., 2016, "Thermoelectric Devices for Power Generation: Recent Progress and Future Challenges " Advanced Engineering Materials, 18(2), pp. 194−213. http://dx.doi.org/10.1002/adem.201500333

[4] He, J., and Tritt, T. M., 2017, "Advances in Thermoelectric Materials Research: Looking Back and Moving Forward," Science, 357(6358), pp. 1369 & eaak9997-1–9. http://dx.doi.org/10.1126/science.aak9997

[5] Chen, R., Lee, J., Lee, W., and Li, D., 2019, "Thermoelectrics of Nanowires," Chemical Reviews, Article ASAP, DOI: 10.1021/acs.chemrev.8b00627. http://dx.doi.org/10.1021/acs.chemrev.8b00627

[6] Li, Y., Liu, M., Liu, K., and Wang, C.-A., 2013, "High Li^+ Conduction in Nasicon-Type $Li_{1+x}Y_xZr_{2-x}(PO_4)_3$ at Room Temperature," Journal of Power Sources, 240(pp. 50–53. http://dx.doi.org/10.1016/j.jpowsour.2013.03.175

[7] Li, Y., Zhou, W., Chen, X., Lü, X., Cui, Z., Xin, S., Xue, L., Jia, Q., and Goodenough, J. B., 2016, "Mastering the Interface for Advanced All-Solid-State Lithium Rechargeable Batteries," Proceedings of the National Academy of Sciences of the United States of America, 113(47), pp. 13313–13317. http://dx.doi.org/10.1073/pnas.1615912113

[8] Yazdani, S., Kashfi-Sadabad, R., Palmieri, A., Mustain, W. E., and Pettes, M. T., 2017, "Effect of Cobalt Alloying on the Electrochemical Performance of Manganese Oxide Nanoparticles Nucleated on Multiwalled Carbon Nanotubes," Nanotechnology, 28(15), pp. 155403-1–11. http://dx.doi.org/10.1088/1361-6528/aa6329

[9] Wu, W., Morales-Acosta, M. D., Wang, Y., and Pettes, M. T., 2019, "Isotope Effect in Bilayer WSe_2," Nano Letters, 19(3), pp. 1527–1533. http://dx.doi.org/10.1021/acs.nanolett.8b04269

[10] Pettes, M. T., Ji, H. X., Sadeghi, M. M., Jo, I., Wu, W., Ruoff, R. S., and Shi, L., 2015, "Scattering of Phonons by High-Concentration Isotopic Impurities in Ultrathin Graphite," Physical Review B, 91(3), pp. 035429-1−13. http://dx.doi.org/10.1103/PhysRevB.91.035429

[11] Vuong, T. Q. P., Liu, S., Van Der Lee, A., Cuscó, R., Artús, L., Michel, T., Valvin, P., Edgar, J. H., Cassabois, G., and Gil, B., 2017, "Isotope Engineering of Van Der Waals Interactions in Hexagonal Boron Nitride," Nature Materials, 17, pp. 152–158. http://dx.doi.org/10.1038/nmat5048

[12] Cuscó, R., Artús, L., Edgar, J. H., Liu, S., Cassabois, G., and Gil, B., 2018, "Isotopic Effects on Phonon Anharmonicity in Layered Van Der Waals Crystals: Isotopically Pure Hexagonal Boron Nitride," Physical Review B, 97(15), pp. 155435-1–12. http://dx.doi.org/10.1103/PhysRevB.97.155435

[13] Li, X., Zhang, J., Puretzky, A. A., Yoshimura, A., Sang, X., Cui, Q., Li, Y., Liang, L., Ghosh, A. W., Zhao, H., Unocic, R. R., Meunier, V., Rouleau, C. M., Sumpter, B. G., Geohegan, D. B., and Xiao, K., 2019, "Isotope-Engineering the Thermal Conductivity of Two-Dimensional MoS_2," ACS Nano, 13(2), pp. 2481–2489. http://dx.doi.org/10.1021/acsnano.8b09448

[14] Lindsay, L., Broido, D. A., and Reinecke, T. L., 2012, "Thermal Conductivity and Large Isotope Effect in GaN from First Principles," Physical Review Letters, 109(9), pp. 095901-1–5. http://dx.doi.org/10.1103/PhysRevLett.109.095901

[15] Lowhorn, N. D., Wong-Ng, W., Zhang, W., Lu, Z. Q., Otani, M., Thomas, E., Green, M., Tran, T. N., Dilley, N., Ghamaty, S., Elsner, N., Hogan, T., Downey, A. D., Jie, Q., Li, Q., Obara, H., Sharp, J., Caylor, C., Venkatasubramanian, R., Willigan, R., Yang, J., Martin, J., Nolas, G., Edwards, B., and Tritt, T., 2009, "Round-Robin Measurements of Two Candidate Materials For a Seebeck Coefficient Standard Reference Material™," Applied Physics A, 94(2), pp. 231−234. http://dx.doi.org/10.1007/s00339-008-4876-5

[16] Wang, H., Mccarty, R., Salvador, J. R., Yamamoto, A., and König, J., 2014, "Determination of Thermoelectric Module Efficiency: A Survey," Journal of Electronic Materials, 43(6), pp. 2274−2286. http://dx.doi.org/10.1007/s11664-014-3044-2

[17] Wang, H., Porter, W. D., Böttner, H., König, J., Chen, L., Bai, S., Tritt, T. M., Mayolet, A., Senawiratne, J., Smith, C., Harris, F., Gilbert, P., Sharp, J. W., Lo, J., Kleinke, H., and Kiss, L., 2013, "Transport Properties of Bulk Thermoelectrics—an International Round-Robin Study, Part

I: Seebeck Coefficient and Electrical Resistivity," Journal of Electronic Materials, 42(4), pp. 654−664. http://dx.doi.org/10.1007/s11664-012-2396-8

[18] Snyder, G. J., and Toberer, E. S., 2008, "Complex Thermoelectric Materials," Nature Materials, 7(2), pp. 105–114. http://dx.doi.org/10.1038/nmat2090

[19] Kraemer, D., Jie, Q., Mcenaney, K., Cao, F., Liu, W., Weinstein, L. A., Loomis, J., Ren, Z., and Chen, G., 2016, "Concentrating Solar Thermoelectric Generators with a Peak Efficiency of 7.4%," Nature Energy, 1, pp. 16153-1–8. http://dx.doi.org/10.1038/nenergy.2016.153

[20] Elson, A., Tidball, R., and Hampson, A., 2015, *Waste Heat to Power Market Assessment*, ICF International, Fairfax, Virginia. http://info.ornl.gov/sites/publications/Files/Pub52953.pdf

[21] Kim, H. S., Liu, W., Chen, G., Chu, C.-W., and Ren, Z., 2015, "Relationship between Thermoelectric Figure of Merit and Energy Conversion Efficiency," Proceedings of the National Academy of Sciences of the United States of America, 112(27), pp. 8205–8210. http://dx.doi.org/10.1073/pnas.1510231112

[22] Wang, H., Bai, S., Chen, L., Cuenat, A., Joshi, G., Kleinke, H., König, J., Lee, H. W., Martin, J., Oh, M.-W., Porter, W. D., Ren, Z., Salvador, J., Sharp, J., Taylor, P., Thompson, A. J., and Tseng, Y. C., 2015, "International Round-Robin Study of the Thermoelectric Transport Properties of an *n*-Type Half-Heusler Compound from 300 K to 773 K," Journal of Electronic Materials, 44(11), pp. 4482−4491. http://dx.doi.org/10.1007/s11664-015-4006-z

[23] Van Der Pauw, L. J., 1958, "A Method of Measuring the Resistivity and Hall Coefficient on Lamellae of Arbitrary Shape," Philips Technical Review, 20, pp. 220–224.

[24] García-Cañadas, J., and Min, G., 2014, "Multifunctional Probes for High-Throughput Measurement of Seebeck Coefficient and Electrical Conductivity at Room Temperature," Review of Scientific Instruments, 85(4), pp. 043906-1−4. http://dx.doi.org/10.1063/1.4871553

[25] He, X., Yang, J., Jiang, Q., Luo, Y., Zhang, D., Zhou, Z., Ren, Y., Li, X., Xin, J., and Hou, J., 2016, "A New Method for Simultaneous Measurement of Seebeck Coefficient and Resistivity," Review of Scientific Instruments, 87(12), pp. 124901-1−6. http://dx.doi.org/10.1063/1.4969056

[26] Kraemer, D., and Chen, G., 2014, "High-Accuracy Direct ZT and Intrinsic Properties Measurement of Thermoelectric Couple Devices," Review of Scientific Instruments, 85(4), pp. 045107-1−9. http://dx.doi.org/10.1063/1.4870278

[27] Mackey, J., Dynys, F., and Sehirlioglu, A., 2014, "Uncertainty Analysis for Common Seebeck and Electrical Resistivity Measurement Systems," Review of Scientific Instruments, 85(8), pp. 085119-1–10. http://dx.doi.org/10.1063/1.4893652

[28] Iwanaga, S., Toberer, E. S., Lalonde, A., and Snyder, G. J., 2011, "A High Temperature Apparatus for Measurement of the Seebeck Coefficient," Review of Scientific Instruments, 82(6), pp. 063905-1–6. http://dx.doi.org/10.1063/1.3601358

[29] Snyder, G. J., 2015, *Measuring Seebeck Coefficient*. United States Patent and Trademark Office, Patent No. 9,140,612 B2. http://pdfpiw.uspto.gov/.piw?Docid=09140612

[30] Yazdani, S., Kim, H.-Y., and Pettes, M. T., 2018, "Uncertainty Analysis of Axial Temperature and Seebeck Coefficient Measurements," Review of Scientific Instruments, 89(8), pp. 084903-1–8. http://dx.doi.org/10.1063/1.5023909

[31] Touloukian, Y. S., and Ho, C. Y., 1970, *Thermophysical Properties of Matter*, IFI/Plenum, New York.

[32] 2002, Graftech Engineering Manual, http://www.graftech.com/

[33] Bergman, T. L., Lavine, A. S., Incropera, F. P., and Dewitt, D. P., 2011, *Fundamentals of Heat and Mass Transfer*, John Wiley & Sons, New York.
http://www.wiley.com/WileyCDA/WileyTitle/productCd-EHEP001810.html

Figure Captions.

Figure 1. Overview of current electro-thermal property characterization methods in comparison with the approach proposed here. The properties that must be obtained to quantify device efficiency for thermal-to-electrical energy interconversion are the electrical conductivity (σ), thermal conductivity (κ), and Seebeck coefficient (S).

Figure 2. (a) Schematic of the high temperature electro-thermal characterization apparatus showing axial thermocouples, heated radiation shield, and actively cooled heat sink. (b-c) Detail of the enabling design components. (d) A detailed top view of the instrument top heat spreader.

Figure 3. The heat flux through the sample for average temperatures of (a) $T = 300$°C and (b) $T = 1000$°C.

Figure 4. (a) Temperature distribution across the instrument with the radiation shield temperature set at 909°C. The upper surface boundary condition was set as thermally insulating and the lower surface was kept at 22°C. (b) Detail of the temperature distribution across the outer surface of the top heat spreader with a maximum variation of 0.45°C.

Figure 5. Temperature distribution for a pyroceram 9606 sample with a thermal conductivity of ~2.9 $Wm^{-1}K^{-1}$ at 907°C. (a) Hot side, (b) cold side, (c) isometric view, and (d) sample surface temperature variation along the radial direction exhibit a maximum value less than 0.01°C above the center point temperature where the thermocouple contacts the sample.

Figure 6. Temperature distribution across the (a) top and (b) bottom thermocouples.

Figure 7. Temperature distribution across (a) the hot surface of the 12.7 mm diameter, 5 mm thick BN sample and (b) the cold surface of the sample. The radiation shield upper and lower half setpoints were 2502 and 2490°C, respectively. (c) Temperature variation across the radial direction on the sample for hot and cold sides illustrates a maximum variation of less than 0.23°C above the center point temperature where the thermocouple contacts the sample. (d) Instrument temperature distribution.

Journal of Heat Transfer. Received August 10, 2018;
Accepted manuscript posted April 24, 2019. doi:10.1115/1.4043572

Figures.

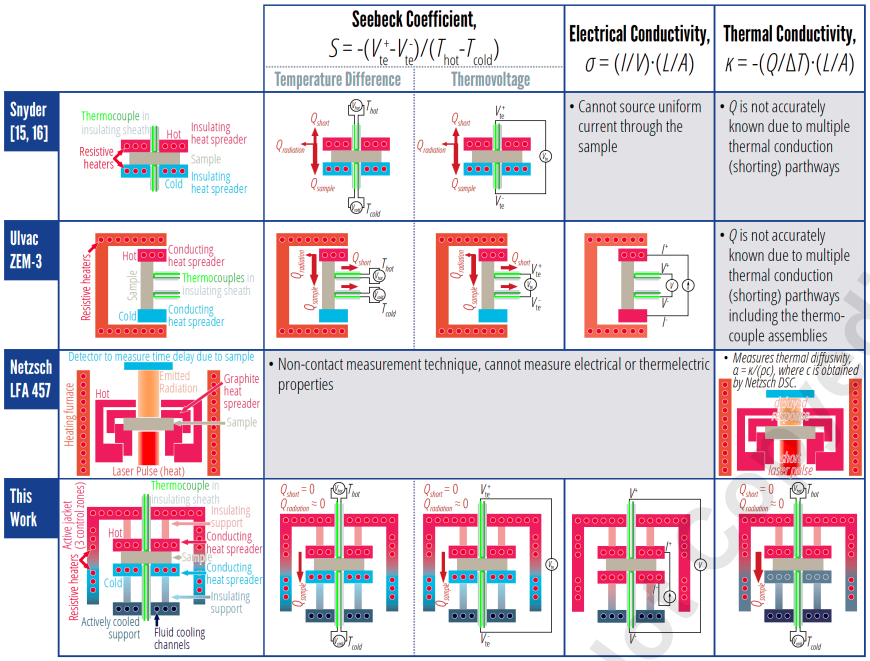

Figure 1:

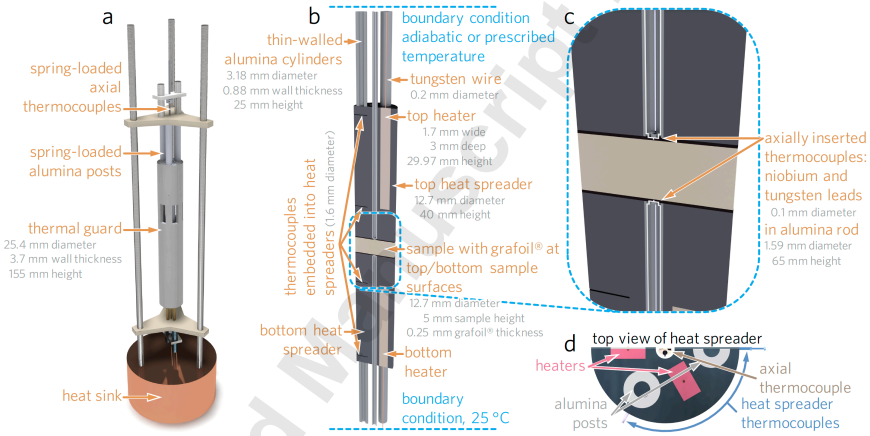

Figure 2:

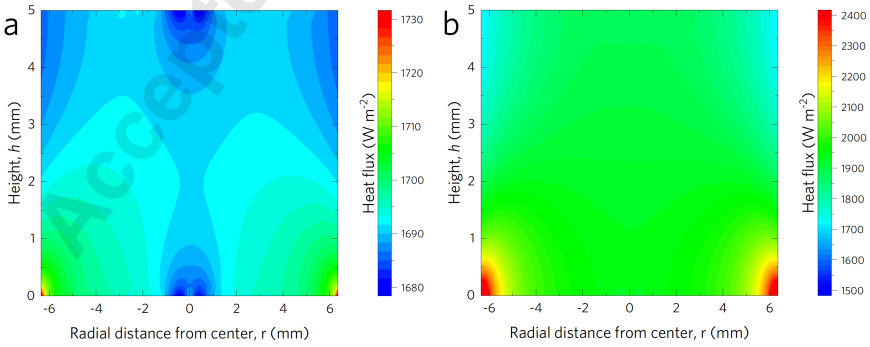

Figure 3:

Journal of Heat Transfer. Received August 10, 2018;
Accepted manuscript posted April 24, 2019. doi:10.1115/1.4043572

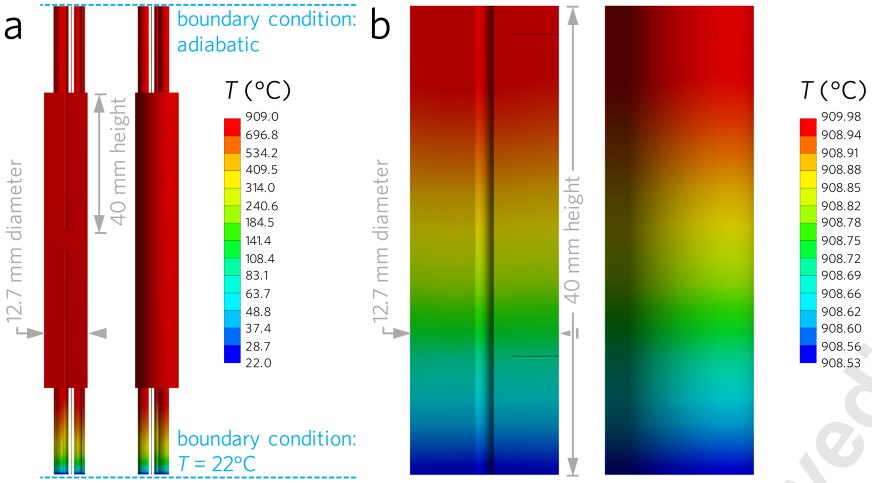

Figure 4:

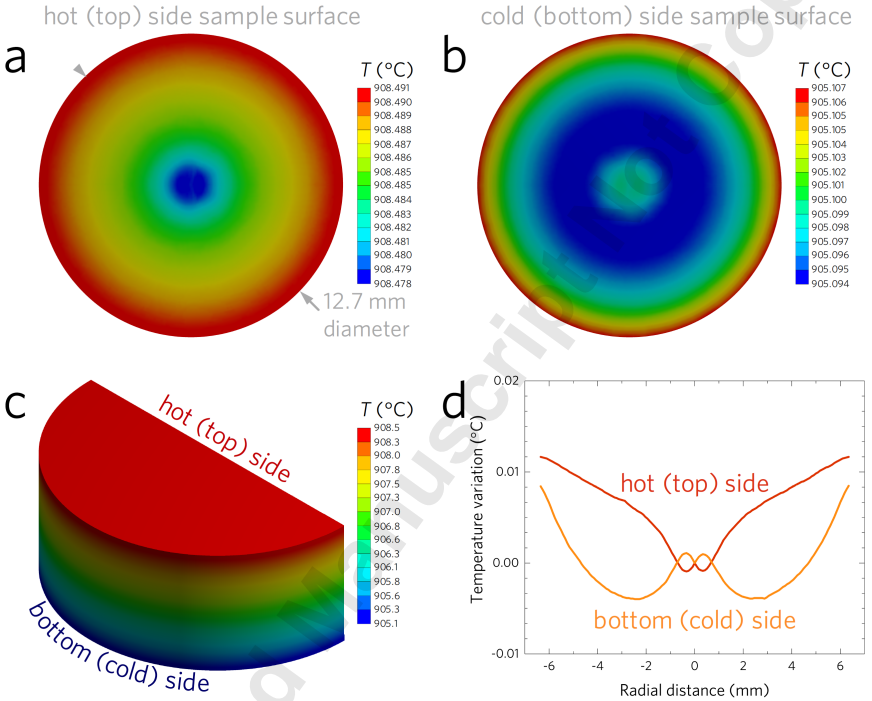

Figure 5:

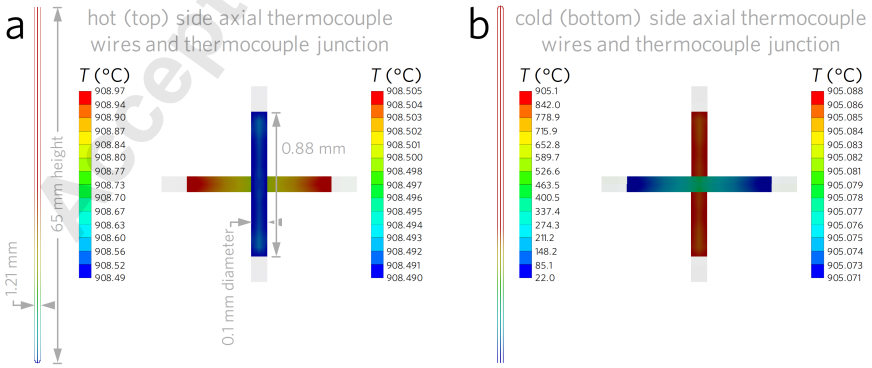

Figure 6:

Journal of Heat Transfer. Received August 10, 2018;
Accepted manuscript posted April 24, 2019. doi:10.1115/1.4043572

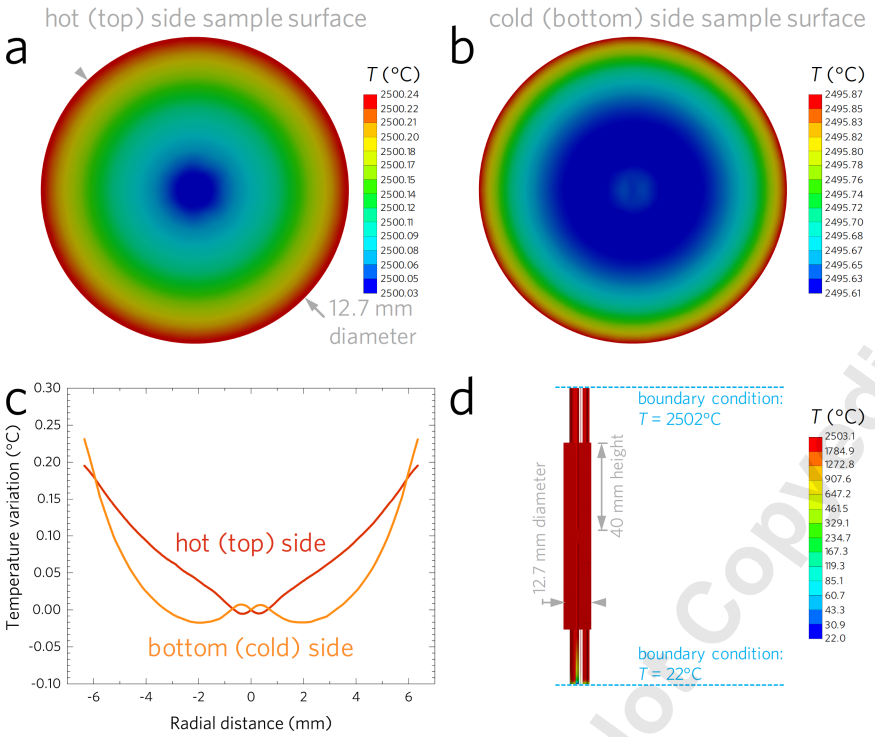

Figure 7:

Table Headings.

Table 1. Uncertainty analysis of the surface temperature distribution and cold-finger effect in Snyder's design [28, 29] obtained by a thermal finite element analysis. T_{hot} and T_{cold} are the top (hot) side and bottom (cold) side temperatures of the sample center, respectively with $\Delta T = T_{hot} - T_{cold}$. The temperature of the radiation shield was kept at 22°C. The radius of the sample and the heat spreader are denoted r_{sample} and $r_{heat\_spreader}$, respectively. The total average temperatures and standard deviations were obtained on the hot and cold surfaces. The uncertainties due to temperature non-uniformity and the cold-finger effect were obtained according to Equations 1 and 2, respectively. The overall uncertainty was calculated according to Equation 3.

Table 2. A comparison between the heater output and the average heat flux through the sample at various temperatures. The specified temperatures indicate the temperature of the sample center on the bottom (cold) surface. The center temperatures of the sample on the hot surface were kept 5°C above these values. The lower values of the top surface heat flux average in comparison with the full surface average indicate the overestimation of the sample heat flux due to radiation.

Table 3. The thermal conductivity error propagated from the temperature probe error, and as the error between the input and the surface average heat flux. The specified temperatures indicate the temperature of the sample center on the bottom (cold) surface. The center temperatures of the sample on the hot surface were kept 5°C above these values. The heat flux and temperature uncertainties were calculated based on Equations 6 and 7, respectively. The propagated thermal conductivity error was calculated according to Equation 8. The direct thermal conductivity error was calculated based a comparison between the κ value obtained from Equation 4 and the input value for the sample used in the model.

Table 4. The thermal conductivity error propagated from the temperature probe error and as the error between the input and the surface average heat flux for the upper instrument surface set as an insulator or set at 915°C. The sample was set to be pyroceram 9606, and the radiation shield was set to 909°C. The heat flux and temperature uncertainties were calculated based on Equations 6 and 7, respectively. The propagated thermal conductivity error was calculated according to Equation 8. The direct thermal conductivity error was calculated based a comparison between the κ value obtained from Equation 4 and the input value for the sample used in the model.

Table 5. The thermal conductivity error propagated from the temperature probe error and obtained as the error between the input and the surface average heat flux for a boron nitride sample at ~2500°C. The specified temperatures refer to the temperature of the sample center on the top (hot) and bottom (cold) surfaces. The heat flux and temperature uncertainties were calculated based on Equations 6 and 7, respectively. The propagated thermal conductivity error was calculated according to Equation 8. The direct thermal conductivity error was calculated based a comparison between the κ value obtained from Equation 4 and the input value for the sample used in the model.

Table 6. The thermal conductivity error propagated from the temperature probe error, and as the error between the input and the surface average heat flux for a boron nitride sample at ~2500°C with a two-stage top radiation shield. The specified temperatures refer to the temperature of the sample center on the top (hot) and bottom (cold) surfaces. The heat flux and temperature uncertainties were calculated based on Equations 6 and 7, respectively. The propagated thermal conductivity error was calculated according to Equation 8. The direct thermal conductivity error was calculated based a comparison between the κ value obtained from Equation 4 and the input value for the sample used in the model.

Journal of Heat Transfer. Received August 10, 2018;
Accepted manuscript posted April 24, 2019. doi:10.1115/1.4043572

Tables.

Table 1:

$r_{sample}/r_{heat\_spreader}$	Sample center surface temperature (°C)			Mean surface temperature (°C)		Standard deviation of $T_{surface}$ (°C)		Uncertainty in temperature (%)		
	T_{hot}	T_{cold}	ΔT	hot side	cold side	hot side	cold side	U_T	$U_{cold\text{-}finger}$	U_{total}
1.00	905.8	901.0	4.8	905.8	900.6	0.73	0.80	8.7	0.4	8.7
	912.7	900.5	12.2	913.0	899.8	0.70	0.87	8.7	0.4	8.8
0.42	905.4	900.9	4.5	905.9	900.9	0.19	0.20	10.1	1.0	10.2
	910.4	899.2	11.2	911.2	898.9	0.47	0.39	10.0	0.5	10.0

Table 2:

Temperature (°C)	100	300	600	800	1000
Heater output (kW m^{-2})	1.53	1.72	1.82	1.97	2.07
Full surface average (kW m^{-2})	1.50	1.69	1.79	1.89	1.92
Top surface average (kW m^{-2})	1.50	1.69	1.77	1.83	1.81

Table 3:

Temperature (°C)	100	300	600	800	1000
Temperature error (%)	0.21	0.26	0.30	0.41	0.65
Heat flux error (%)	2.09	1.66	2.03	4.31	7.64
Propagated thermal conductivity error (%)	2.10	1.68	2.05	4.34	7.66
Direct thermal conductivity error (%)	2.17	2.03	2.19	4.60	8.22

Journal of Heat Transfer. Received August 10, 2018;
Accepted manuscript posted April 24, 2019. doi:10.1115/1.4043572

Table 4:

Model Conditions and Uncertainty Analysis at ~900°C	Value
Sample top surface center temperature (°C) (upper boundary condition, insulating)	908.5
Sample top surface center temperature (°C) (upper boundary condition, T=915°C)	908.6
Sample bottom surface center temperature (°C) (upper boundary condition, insulating)	905.1
Sample bottom surface center temperature (°C) (upper boundary condition, T=915°C)	905.1
Temperature difference error (%)	0.46
Top surface average (kW m^{-2})	1.87
Heater output (kW m^{-2})	1.81
Heat flux error (%)	3.07
Propagated thermal conductivity error (%)	3.10
Direct thermal conductivity error (%) (upper instrument surface insulating)	-7.70
Direct thermal conductivity error (%) (upper instrument surface kept at T=915°C)	-8.60

Table 5:

Model Conditions and Uncertainty Analysis at ~2500°C	Value
Top heat spreader heater power (MW m^{-3})	4
Bottom heat spreader heater power (MW m^{-3})	1
Sample top surface center temperature (°C)	2,500.0
Sample bottom surface center temperature (°C)	2,495.6
Radiation shield upper half set temperature (°C)	2,502.0
Radiation shield lower half set temperature (°C)	2,490.0
Temperature difference error (%)	4.87
Sample top surface average heat flux (kW m^{-2})	14.09
Heater output on the top sample surface (kW m^{-2})	14.48
Heat flux error (%)	2.74
Propagated thermal conductivity error (%)	5.60
Direct thermal conductivity error (%)	-17.15

Journal of Heat Transfer. Received August 10, 2018;
Accepted manuscript posted April 24, 2019. doi:10.1115/1.4043572

Table 6.

Model Conditions and Uncertainty Analysis at ~2500°C with Two Thermal Guards	Value
Top heat spreader heater power (MW m^{-3})	4
Bottom heat spreader heater power (MW m^{-3})	1
Sample top surface center temperature (°C)	2,499.5
Sample bottom surface center temperature (°C)	2,495.3
Radiation shield stage #1 upper set temperature (°C)	2,502.1
Radiation shield stage #2 upper set temperature (°C)	2,500.9
Radiation shield lower half set temperature (°C)	2,490.0
Temperature difference error (%)	4.24
Sample top surface average heat flux (kW m^{-2})	13.98
Heater output on the top sample surface (kW m^{-2})	14.48
Heat flux error (%)	3.56
Propagated thermal conductivity error (%)	5.50
Direct thermal conductivity error (%)	-13.31